Mathematical Modeling and Simulation of Biologically Inspired Hair Receptor Arrays in Laminar Unsteady Flow Separation

B.T. Dickinson*,[a], J.R. Singler[b], B.A. Batten[c]

[a] *Munitions Directorate, Air Force Research Laboratory, 101 W Eglin Blvd, Ste 213 Eglin AFB, FL 32542*
[b] *Department of Mathematics and Statistics, Misourri Institute of Science and Technology, 400 W 12th St, Rolla, MO 65409*
[c] *School of Mechanical, Industrial, and Manufacturing Engineering, Oregon State University, 204 Rogers Hall, Corvallis, OR 97331*

Abstract

Bats possess arrays of distributed flow-sensitive hair-like mechanoreceptors on their dorsal and ventral wing surfaces. It is generally hypothesized that the hair sensor array provides air flow feedback during flight. Specifically, the sensing of leading and trailing edge vortices that are shed during flapping flight has been proposed. In this work, we consider the mechanics of flexible hair-like structures for the time accurate measurement and visualization of hydrodynamic images associated with unsteady near surface flow phenomena. A nonlinear viscoelastic model of a hair-like structure coupled to an unsteady nonuniform flow environment is proposed. Writing the hair model in nondimensional form, we perform an order of magnitude analysis of the physical forces involved in the fluid-structure hair response. Through the proper choice of hair material, we show how the time accurate measurement of near surface flow velocity may be obtained from hair tip displacement and resultant moment. Furthermore, we show how a surface mounted hair array may provide a time accurate hydrodynamic image of a laminar unsteady flow separation over a cylinder.

Key words: micro air vehicles, bats, low Reynolds number, finite elements,

*Corresponding Author
Email addresses: benjamin.dickinson.1@us.af.mil (B.T. Dickinson), singlerj@mst.edu (J.R. Singler), bbatten@engr.orst.edu (B.A. Batten)

hair cell sensors, micropillar, wall shear stress

1. Introduction

Many animals use flow-sensitive hair-like structures to provide information on their environment. Recent studies have shown that bat wings are populated with micro-scale flow-sensitive hairs (Figure 1) (Crowley and Hall, 1994; Zook, 2005). The distinguishing feature of the wing hair receptors from pelage hair

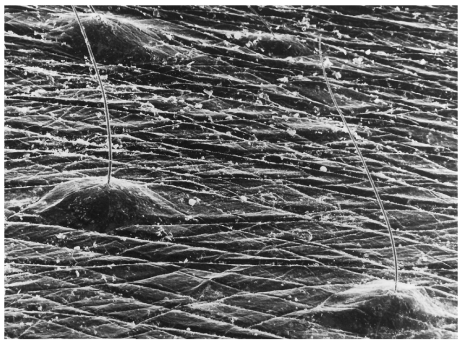

Figure 1: Scanning electron micrograph of bat wing hair receptors on the membrane of *Pteropus poliocephalis* (the grey-headed flying-fox) (Reproduced by permission of CSIRO PUBLISHING, from the Australian Journal of Zoology vol. 42(2): 215-231 (GV Crowley and LS Hall). Copyright CSIRO 1994 .http://www.publish.csiro.au/nid/91/issue/2300.htm)

is their concentration of touch sensitive cells in dome-shaped complexes at the hair base. Upon hair ablation, flight behavior is clearly altered with evidence of reduced maneuverability (Zook, 2005; Sterbing-D'Angelo et al., 2008). This has led biologists to hypothesize that bat wing hair receptors feedback airflow information for aerodynamic control. Specifically, Zook (2005) proposed turbulent boundary layer feedback while Sterbing-D'Angelo et al. (2008) suggested the sensing of leading and trailing edge vortices, which are periodically shed during the flapping flight of bats (Hubel et al., 2010). In this work, we consider the mechanics of flexible hair-like structures for the time and space accurate measurement of near surface unsteady flow phenomena.

The measurement of near surface flow patterns (hydrodynamic image) has

been previously considered with passive surface mounted hair-like structures ("micro-pillars") (Brüker et al., 2005; Brücker et al., 2007; Gnanimanickam and Sullivan, 2008). Therein, hair tip displacement is optically tracked to determine the near surface flow velocity and wall shear stress. From the surface velocity and wall shear stress, a time resolved "flow footprint" or topology of the unsteady airflow may be obtained. While this concept is proposed as an analysis tool for experimental fluid mechanics, such measurements may also play a role in achieving agile and maneuverable flight in small scale aircraft.

The agility and maneuverability of aircraft that share the low Reynolds number regime of bats (chord Reynolds numbers $\lesssim 10^6$)[1] is, in part, limited by challenges associated with obtaining an accurate aerodynamic model for control in unsteady flight conditions. This stems from unsteady aerodynamic forces present in low Reynolds number flight regimes (Lissaman, 1983; Shyy et al., 1999; Mueller and DeLaurier, 2005). As an additional aerodynamic observable, the surface measurement of topological features in a flow (lines of separation, reattachment, stagnation) and their relationship to unsteady aerodynamic forces has been considered (Mangalam and Moes, 2004; Mangalam et al., 2008, 2010). For this purpose, the topological feedback of the passive hair-like structures, their scalability, and small footprint make the artificial hair sensor (Figure 2, see also Engel et al. (2005, 2006); Yang et al. (2007); Ozaki et al. (2000); Dijkstra et al. (2005); Schmitz et al. (2005)) an attractive candidate.

Whatever the application, the hair structure response in a flow medium will depend on characteristics of the flow environment, hair geometry, and hair material properties. Thus, ensuring accurate measurement of flow topology with hair-like structures (or ensuring effectiveness in other applications such as measurement of boundary layers, turbulence, or acoustic waves) requires an understanding of hair behavior with respect to material, geometry, and environment.

The mathematical analysis of flow-sensitive hair appears to have begun with

[1] Throughout, the symbol $\sim$ is used to denote orders of magnitude and will be used with inequalities. For example, the symbol $\lesssim$ denotes an order of magnitude or less

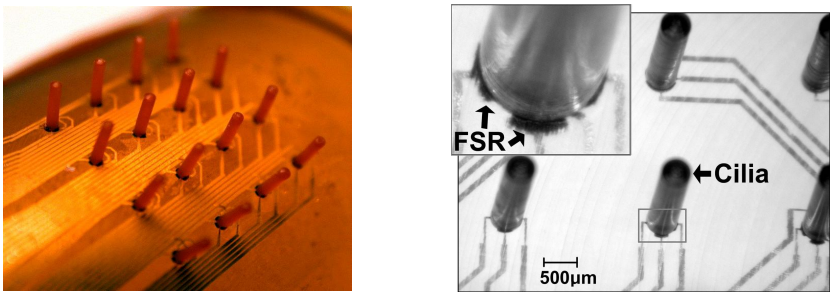

Figure 2: Photo of polymer artificial hair sensor (left) and force sensitive resistor (FSR) at base of polymer AHC (right). *Figures courtesy of C. Liu and group, MNTR lab, Northwestern University*

Tautz (1977) who modeled the caterpillar hair receptor as a rigid damped harmonic oscillator. Refined models were later proposed by Fletcher (1978) for caterpillars, Shimozawa and Kanou (1984) for crickets and cockroaches, and Humphrey et al. (1993) for spiders. Therein, hair receptor function is studied within the context of a specific animal so that the determination of suitable geometric and material parameters is needed for accurate modeling. Although the challenges of hair sensor fabrication at the microscale of the hair receptor have been met, little is known on the implications of hair material selection.

We propose a nonlinear viscoelastic model of a hair-like structure coupled to an unsteady nonuniform flow environment. Through nondimensional analysis and simulation, we show how the time accurate measurement of near surface flow velocity is dependent on hair material properties. Furthermore, we show how the forces in the fluid-structure hair response can be controlled through the choice of hair material. From this understanding, we show how arrays of flexible hair-like structures can provide a space and time accurate representation of near surface flow phenomena with simulations of a flexible hair array in a laminar unsteady flow separation over a cylinder.

2. Mathematical Modeling of the Hair/Fluid Problem

We consider an array of hair-like structures mounted normally to the surface of a fixed half cylinder at 1°, 2°, ..., 179° (Figure 3) that experiences an impulsively started airflow (equivalently, an impulsively started cylinder in quiescent air). In this situation, an unsteady separation is known to occur on the

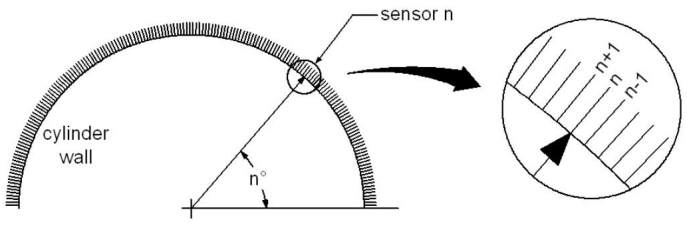

Figure 3: Illustration of hair sensor array position and numbering where sensors are placed at $n = 1°, 2° \ldots, 179°$ measured from the horizontal plane (sensor length and diameter are not shown to scale)

downstream side of the impulsively started cylinder. Here, our interest in the impulsively started flow is mainly for purpose of detecting the sequence of fluid dynamic events from the resulting unsteady separation. For more information on the impulsively started cylinder problem see Sears and Telionis (1975); Cebeci (1979) or Schlichting and Gersten (2000). Numerical details and simulation results of the impulsively started flow will be discussed further in Sections 3 and 4.1.

Each hair structure is modeled as a viscoelastic cantilever beam with uniform diameter and material properties. While this may be consistent with artificial hairs (Figure 2), it is an approximation to the tapered bat wing hair receptor (Figure 1) for which homogeneity and material composition is unknown. A characteristic diameter of bat wing hair receptors (and used for simulations herein) is 1×10^{-5} m. Assuming the hair is subject to flow velocities $\lesssim 10^1$ m/s leads to hair Reynolds numbers of $\lesssim 10^1$ based on diameter. To experience this ratio of inertial to viscous forces, we would need to immerse ourselves in a pool of glycerin and swim at speeds ~ 10 m per hour! From this perspective we anticipate a small influence of hair inertia on dynamic response but still

include inertial terms in the hair model for generality and completeness. We also include the effect of relative velocity and acceleration between the hair structure and airflow. Added mass effects are also considered following their reported importance in the dynamic response of spider trichobothria in oscillatory flows (Humphrey et al., 1993). While the hairs are separated in 1° increments (Figure 3), we do not account for viscous coupling effects that may occur between hairs during the unsteady separation. Although the topic of viscous coupling is not completely understood, further discussion may be found in Bathellier et al. (2005) and Hagedoorn (2008).

We characterize the mechanical response of the hair structure to its surrounding flow medium through tip deflection and the resultant moment at the hair base. Although previous mathematical studies of hair mechanoreceptors use tip deflection to interpret hair response, we note that the instantaneous hair deflection is not necessarily related to the corresponding electrical response output by an artificial hair sensor. This becomes clear when considering a rigid hair structure with zero deflection in a flow where surface forces produce a nonzero resultant moment and shear force at the base of the hair. Clearly, a resultant moment and shear force may induce a response in a substrate mounted MEMS device. Furthermore, such moment and shear force is a potential source of mechanical stress in the bat wing membrane to activate the touch sensitive cells in the hair receptor dome. We will explore the difference in the relationship between local flow velocity, hair deflection and resultant moment in Section 4.2.

Our approach to compute the reaction of a hair array to a viscous unsteady airflow contains three main parts and is similar in approach to simulations performed for cochlear hair cells by Billone and Raynor (1973):

1. The simulation of the flow environment and the extraction of the near surface flow velocity data
2. The simulation of the hair response where surface forces are approximated with interpolated flow data obtained from the previous step
3. The determination of the tip deflection and calculation of moment at the

base of the hair

We note that between Steps 1 and 2, a true fluid-structure interaction (FSI) is not considered (specifically, the effect of the hair-structure on the flow). Instead, we propose a fluid-structure *reaction* (FSR) model of the hair. Our aim is a computationally tractable and accurate mathematical model of a flexible hair-structure in an unsteady fluid flow. After proposing a hair model, we will perform an order of magnitude analysis for a general perspective of the hair structure response in unsteady flows (Sections 2.3 and 4.2). As we discuss in Section 2.2, the coefficients of drag and inertia that describe the forces due to the fluid-structure coupling are not well known. For purpose of better estimating these coefficients, physical experimentation or a computational studies with true FSI are needed.

2.1. Impulsively Started Flow Over a Half Cylinder

The approximation of solutions for the impulsively started flow over a half cylinder is performed in an artificial domain (Figure 4) following the governing equations and boundary conditions provided by Gresho and Sani (1998). Let

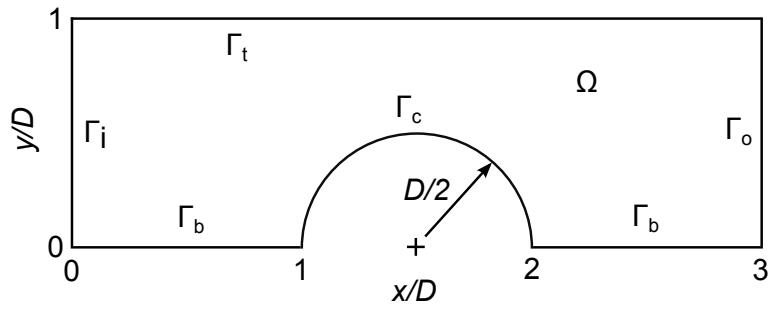

Figure 4: Fluid domain for unsteady fluid separation simulations performed in this analysis.

$\mathbf{u}(t, \mathbf{x}) = [u(t, x, y), v(t, x, y)]$ denote the velocity fields and $p(t, \mathbf{x})$ denote the pressure field that describes the fluid dynamics in Ω modeled by the viscous incompressible form Navier-Stokes equations posed in nondimensional form as

$$\begin{aligned} \mathbf{u}_t + \mathbf{u} \cdot \nabla \mathbf{u} &= \nabla p + \frac{1}{\mathrm{Re}} \nabla^2 \mathbf{u} \\ \nabla \cdot \mathbf{u} &= 0 \end{aligned} \tag{1}$$

with the following dimensionless boundary and initial conditions,

$$\begin{aligned}
u = (1 - e^{-\lambda\, t}),\ v = 0 \qquad & \text{on} \qquad \Gamma_i \quad \times \quad (0, T], \\
-p\,\mathbf{n} + \frac{1}{\mathrm{Re}}\frac{\partial \mathbf{u}}{\partial \mathbf{n}} = 0 \qquad & \text{on} \qquad \Gamma_o \quad \times \quad (0, T], \\
\frac{\partial u}{\partial \mathbf{n}} = 0,\ v = 0 \qquad & \text{on} \qquad \Gamma_{t,b} \quad \times \quad (0, T], \\
\mathbf{u} = 0 \qquad & \text{on} \qquad \Gamma_c \quad \times \quad (0, T], \\
\mathbf{u}(0, \mathbf{x}) = 0 \qquad & \text{in} \qquad \Omega,
\end{aligned}$$

and Reynolds number,

$$\mathrm{Re}_{cyl} = \frac{U_{in}\, D}{\nu}, \tag{2}$$

where U_{in} (= 0.0794 m/s) is a maximum inlet velocity, D (= 0.1 m) is the diameter of the cylinder, and ν is the kinematic viscosity of air so that flow domain Reynolds number Re_{cyl} = 500. Here, the time dependent boundary condition at the inlet Γ_{i} accelerates the uniform inlet flow to a maximum velocity U according to the rate parameter λ (= 15 s^{-1}). The "do nothing" boundary condition (Heywood et al., 1996) was imposed at the outlet Γ_{o}, symmetry boundaries were specified on the top Γ_{t} and bottom Γ_{b} of the domain, and a no-slip condition was set on the surface of the cylinder Γ_{c}.

2.2. Viscoelastic Hair Forced by an Unsteady Viscous Flow

We consider a flexible high aspect ratio ($\ell/d \geq 100$) prismatic circular cylinder rigidly mounted normal to a substrate and forced by a non-uniform unsteady normally incident flow velocity profile. This situation is illustrated in Figure 5, where $g(t, \xi)$ is the surface force per unit length due to hair motion and the incident flow, and $r(t, \xi)$ is the instantaneous hair displacement, for $t > t_0$ and $0 \leq \xi \leq \ell$.

To describe the dynamic and mechanical response of the flexible hair we consider the following force balance

$$F_I + F_E + F_M = F_D + F_A, \tag{3}$$

where F_I is the hair inertial force, F_E represents the hair internal elastic force, F_M is the hair internal force due to material damping, F_D is the external force

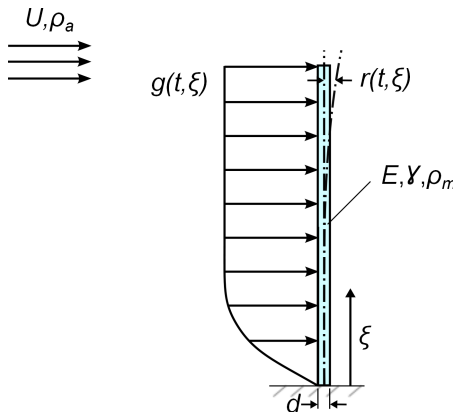

Figure 5: Illustration of the hair-like structure problem considered herein

due to drag, and F_A represents forces due to changes in flow inertia. In modeling the internal forces, we assume that hair tip displacement is less than 10% of its length, following back of the envelope calculations of steady hair deflection in the Blasius boundary layer flow at 10 m/s. Thus, linear Euler-Bernoulli beam theory is a valid approximation of the left hand side of (3). This leads to the following partial differential equation (Inman, 2008)

$$\begin{aligned} \rho_m\, A(\xi)\, r_{tt}(t,\xi) + \gamma\, I(\xi) r_{t\xi\xi\xi\xi}(t,\xi) + \\ E(\xi)\, I(\xi)\, r_{\xi\xi\xi\xi}(t,\xi) = g(t,\xi), \quad 0 < \xi < \ell, \quad t > 0, \end{aligned} \tag{4}$$

with cantilever boundary conditions

$$\begin{aligned} r(t,0) = 0, \quad r_\xi(t,0) = 0, \\ EIr_{\xi\xi}(t,\ell) + \gamma I r_{t\xi\xi}(t,\ell) = 0, \quad EIr_{\xi\xi\xi}(t,\ell) + \gamma I r_{t\xi\xi\xi}(t,\ell) = 0, \end{aligned} \qquad t > 0,$$

and initial conditions

$$\begin{aligned} r(0,\xi) &= r_0(\xi) \\ r_t(0,\xi) &= r_{t\,0}(\xi) \end{aligned}, \quad 0 \le \xi \le \ell.$$

Above (4), ρ_m is the density of the hair; A is cross-sectional area; E is Young's modulus; I is the second moment of area; γ is the Kelvin-Voigt coefficient of material damping; g is the external force per unit length or load intensity due to

the flow; and the subscripts $(\cdot)_\xi$ and $(\cdot)_t$ denote partial derivatives. The moment at the base of the hair is computed from the solution of (4) as

$$M(t) = EIr_{\xi\xi}(t,0) + \gamma Ir_{t\xi\xi}(t,0). \tag{5}$$

In approximating the hair surface forces, we assume axial loads are small compared to the forces acting normal to the longitudinal axis. We approximate the distributed load by considering the net instantaneous force acting *inline* with the one-dimensional motion of the hair cross section at the longitudinal location, ξ (Figure 6). We note that following the small displacement assumption

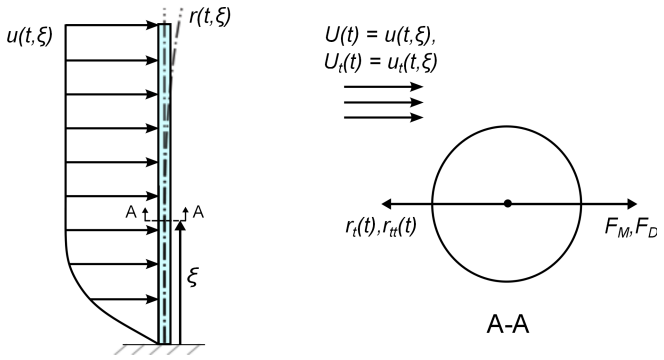

Figure 6: The net surface force on the hair acting at ξ

$(r(\ell,t) < 0.1\,\ell)$, we assume negligible cross sectional eccentricity that would be introduced by the hair deflection from the perspective of the incident flow. If the cylinder diameter is small compared to the wavelength of the incident flow, then at ξ, the *local* flow velocity, $u(t,\xi) = u(t)$, is taken as the instantaneous reference velocity so that $U(t) = u(t)$. Similarly, we define the local instantaneous reference acceleration as $u_t(t,\xi) = U_t(t)$. Combined with the hair velocity, $r_t(\xi,t) = r_t(t)$, and acceleration, $r_{tt}(\xi,t) = r_{tt}(t)$, we estimate the inline force at ξ with Morison's equation (Morison et al., 1950),

$$g(t,\xi) \approx \rho_f\, A\, U_t \,+\, \rho_f\, A\, C_m\,(\,a_r\,) \,+\, \frac{1}{2}\,\rho_f\, d\, C_D\,(\,u_r\,)\,|\,u_r\,|, \tag{6}$$

where the first term is known as the Froude-Krylov force and is due to the outer flow field acceleration, the second term is the hydrodynamic mass force due to

the acceleration of the near surface flow by pressure forces in the vicinity of the accelerating body, and the rightmost term is the drag force. In (6), ρ_f is the flow density, C_m is the hydrodynamic mass coefficient (also referred to here as the inertial coefficient), C_D is the coefficient of drag, $u_r(t) = U(t) - r_t(t)$ is the relative flow velocity, and $a_r(t) = U_t(t) - r_{tt}(t)$ is the relative acceleration.

Morison's equation (6) was originally proposed to estimate wave loads on ocean piles. Since its introduction, questions on accuracy and validity have led to an extensive body of research on the hydrodynamics of cylindrical structures in oscillating flows. Although the difference in scale between an ocean piling and a hair-like structure is enormous, their geometry and environment are similar (high aspect ratio cylindrical structure in a viscous, nonuniform, and unsteady flow). It follows that much of the knowledge base historically applied to pilings is also relevant to the hair-like structure. Below, we briefly discuss the corresponding data. A comprehensive source of information on the fluid mechanics and dynamics over cylindrical structures may be found in the books by Sarpkaya and Issacson (1981) and Sumer and Fredsøe (2006).

Morison's equation (6) uses a linear superposition of inertial and drag forces to approximate surface forces over a cylindrical body in a viscous, nonuniform, and unsteady flow. It is important to note that when the flow over the cylinder is unsteady, the drag and inertial coefficients may not only depend on the Reynolds number (as for the steady flow case), but potentially other nondimensional groups.

In the sinusoidally oscillating flow ($U(t) = U_m \sin(\omega\, t)$), the drag and inertial coefficients depend on the Reynolds number,

$$\mathrm{Re} = \frac{U_m\, d}{\nu}, \tag{7}$$

and the Keulegan-Carpenter number (Keulegan and Carpenter, 1958),

$$KC = \frac{U_m\, T}{d}, \tag{8}$$

where $T = 1/\omega$ is the period of the oscillatory flow.

The Keulegan-Carpenter number indicates the relative importance of the

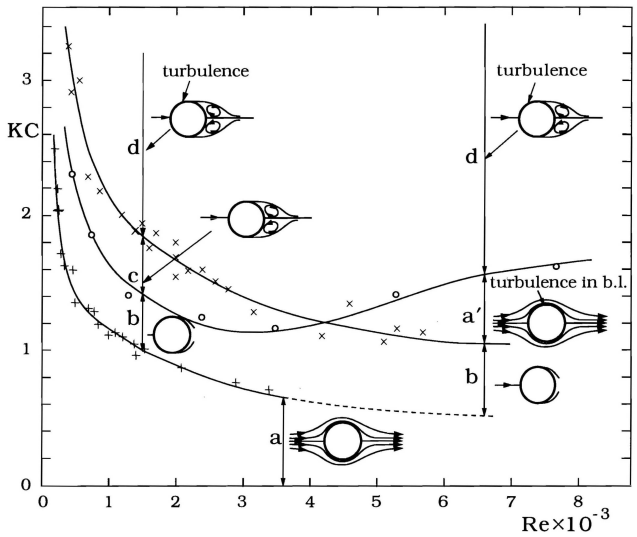

Figure 7: The regimes of flow around a smooth circular cylinder in oscillatory flow for small KC numbers (KC < 3). The various flow regimes in this figure are: a: No separation, b: Separation with Honji vortices, c: A pair of symmetric vortices, and d: A pair of symmetric vortices, but turbulence over the cylinder surface. Data: Circles from Sarpkaya (1986); crosses for Re < 1000 from Honji (1981) and crosses from Sarpkaya (1986). This diagram is adapted from Sarpkaya (1986) and reproduced by permission of WORLD SCIENTIFIC PUBLISHING from Hydrodynamics Around Cylindrical Structures (Sumer and Fredsøe), Copyright WORLD SCIENTIFIC PUBLISHING 1997

drag and inertial forces. Alternatively, KC may be expressed as the amplitude of fluid motion, a, to the cylinder diameter, KC $= 2\,\pi\,a/d$. Figure 7 illustrates the various flow regimes observed over a cylinder in the sinusoidally oscillating flow over the parameter space of Re and KC. The curve between regions a and b show that the onset of separation asymptotically approaches Re=5 as KC $\rightarrow \infty$, which is expected in order to reconcile with the case of attached flow in the steady current when Re$\leq$5 (Sumer and Fredsøe, 2006). From Figure 7, we expect the flow over a 10 μm diameter hair to remain *attached* for $u_r \lesssim 8$ m/s (at 300K, neglecting any potential end effects).

We note for attached flow, the oscillatory and steady reference scenarios do not necessarily imply common drag and inertial coefficients. For the most

accurate estimation of surface forces over the hair structure, the drag and inertial coefficients should be determined with respect to the most appropriate reference scenario.

For hair-like structures in an acoustic wave without a superimposed current, a suitable reference condition is the sinusoidally oscillating flow. However, here we investigate the hair response at various locations in an unsteady separation over a half cylinder, where depending on hair location, the flow may be best represented by a steady current or oscillatory flow. In fact, the steady and oscillatory reference conditions are special cases of their superposition, $U(t) = U_c + U_m \sin(\omega\, t)$, where $U_c/U_m \to \infty$ is effectively the steady case and $U_c/U_m = 0$ is the oscillating reference condition. Indeed, this reference condition has been previously studied (see (Sumer and Fredsøe, 2006) and the references therein) although at the regime of ocean pilings where Re$\sim 10^3$ to 10^4. To our knowledge, no drag or inertial data exists for this reference condition over the attached flow regime $\mathrm{Re}_\xi \leq 5$.

Lacking this data, we assume that within the regime of attached flow the instantaneous drag force may be approximated from coefficients for steady flow over the cylinder. For this purpose, we define the instantaneous local Reynolds number,

$$\mathrm{Re}_\xi = \frac{|U(t) - r_t(t)|\, d}{\nu}. \tag{9}$$

For creeping flows ($\mathrm{Re}_\xi << 1$), we approximate C_D with Lamb's analytical formula (Lamb, 1911) for the drag coefficient over a cylindrical cross-section,

$$C_D = \frac{8\pi}{\mathrm{Re}_\xi \, \ln(\frac{37}{5\,\mathrm{Re}_\xi})}, \tag{10}$$

which is in good agreement with experimental data for Re_ξ up to 0.5 (see Prandtl (1952) p. 191). At larger Reynolds numbers, empirical relationships may be developed. A least squares fit to the drag coefficient data for the cylinder in cross-flow at $\mathrm{Re}_\xi = 10^{-1}$, 10^0, and 10^1 (based on data in Prandtl (1952) p. 190) leads to the following linear logarithmic relationship

$$\ln C_D(\mathrm{Re}_\xi) = -\frac{2}{3} \ln(\mathrm{Re}_\xi) + \frac{5}{2} \tag{11}$$

with an R-squared value of 0.996.

The above formulae assumed an infinite cylinder in cross-flow and does not account for end effects due to the finite length hair structure. However, previous computational studies of 10:1 and 200:1 aspect ratio micro-cantilevers in steady cross flow for $1 \leq \mathrm{Re} \leq 63$ show that C_D varies by less than 5%, indicating that end effects are small (Jana et al., 2007). Therein, over $1 \leq \mathrm{Re} \leq 63$, the quadratic logarithmic relationship

$$\ln C_D(\mathrm{Re}_\xi) = 2.794 - 0.8036 \ln(\mathrm{Re}_\xi) + 0.05500 \ln^2(\mathrm{Re}_\xi) \tag{12}$$

provides an excellent fit to simulation data.

Finally, we take the potential flow value of the hydrodynamic mass coefficient, $C_m = 1$, neglect lift, and neglect torsion, following the assumption of attached flow over the hair cross section ($\mathrm{Re}_\xi \leq 5$).

2.3. Nondimensional Form of Dynamic Hair Model

To write the hair model (4) in nondimensional form, we scale the variables ξ, r, t, and u as

$$\xi' = \frac{\xi}{\ell}, \quad r' = \frac{r}{d}, \quad t' = \frac{t}{T_f}, \quad u' = \frac{u_n}{U}, \tag{13}$$

where $U = U_{in}$ (the equilibrium inlet velocity from the flow inlet condition 1), T_f is a characteristic unsteady time scale of the flow, taken here as $T_f = 1/\lambda$ where λ is the inlet acceleration parameter defined in Section 2.1.

The transformation of the hair structure model (4) with the dimensionless variables (13) leads to the following equivalent form

$$\begin{aligned} \frac{\rho_m A}{T_f^2} r'_{t't'} + \frac{E I d}{\ell^4} r'_{\xi'\xi'\xi'\xi'} + \frac{\gamma I d}{T_f \ell^4} r'_{\xi'\xi'\xi'\xi'} = \\ \frac{\rho_f A U}{T_f} u'_{t'} + \frac{\rho_f A U C_m}{T_f} \left(u'_{t'} - \frac{d}{U T_f} r'_{t't'} \right) + \\ \frac{1}{2} \rho_f d C_D U^2 \left(u' - \frac{d}{U T_f} r'_{t'} \right) \left| u' - \frac{d}{U T_f} r'_{t'} \right|. \end{aligned} \tag{14}$$

To further analyze the coefficients of (14), we first define several reference quantities, listed in Table 2.3. The material time scale, T_m, is a characteristic time

Table 1: List of reference variables related to the nondimensional transformation of the hair structure model

Variable	Description
$T_m = \frac{\gamma}{E}$	Hair material time scale
$q = \rho_a U^2$	Reference Dynamic pressure
$A_f = d\,\ell$	Hair frontal area
$R = \frac{\ell}{d}$	Hair aspect ratio
$g_r = \frac{q\,A_f}{\ell}$	Reference load intensity
$T_i = \sqrt{\frac{m}{g_r}}$	Hair inertia time scale
$M_r = \frac{1}{2}\,g_r\,\ell^2$	Reference resultant moment
$m = \rho_s\,A\,\ell$	Hair mass
$\rho_r = \frac{E\,I}{M_r}$	Reference radius of curvature

period of material relaxation. The inverse, T_m^{-1}, is known as the *rate of relaxation* and indicates the rate that strain in a viscoelastic material comes to equilibrium due to an applied stress (Davis, 1987). The reference load intensity, g_r, is the uniform force per hair unit length due to the reference stagnation pressure $q = \rho_a\,U^2$. With g_r, we may determine the inertial time scale, $T_i = \sqrt{m/g_r}$. It can be shown that T_i is the period for a body of mass m (the hair mass) and characteristic size d initially at rest and acted only upon by the reference load intensity g_r to move a distance d. The reference load, $g_r \cdot \ell$, creates the reference

resultant moment, $g_r \ell^2/2$, leading to the reference radius of curvature $E\,I \backslash M_r$.

We write equation (14) in nondimensional form by dividing through by one-half the reference load intensity, $g_r/2$, to obtain

$$\begin{aligned} \left[\frac{2}{R}\,\Lambda^2 + \frac{\pi}{2}\,\Phi\,C_m\right]\,r_{tt}\;+\;\frac{\Gamma}{R}\,\left(r_{\xi\xi\xi\xi}\;+\;\Psi\,r_{t\xi\xi\xi\xi}\right) = \\ \frac{\pi}{2}\,\left(1+C_m\right)\,\Phi\,u_t\;+C_D\,\left(u-\Phi\,r_t\right)\,|u-\Phi\,r_t| \end{aligned} \tag{15}$$

with boundary conditions

$$\begin{aligned} r(t,0)=0, \quad r_\xi(t,0)=0, \\ r_{\xi\xi}(t,1)+\Psi\,r_{t\xi\xi}(t,1)=0, \quad r_{\xi\xi\xi}(t,1)+\Psi\,r_{t\xi\xi\xi}(t,1)=0, \end{aligned} \qquad t>t_0,$$

and initial conditions

$$\begin{aligned} r(0,\xi)=r_0(\xi) \\ r_t(0,\xi)=r_{t\,0}(\xi) \end{aligned} \quad , \quad 0\le\xi\le 1.$$

The nondimensional resultant moment at the base of the hair is now

$$M = r_{t\xi\xi}(t,0)\;+\Psi\,r_{\xi\xi}(t,0) \tag{16}$$

where the scaling moment is R/K and $K=EI/\ell$ is the flexural stiffness. Note that for notational simplicity, we have omitted the prime denoting the nondimensional variables. We will continue this practice throughout the remained of this paper. The capital Greek letters in (15) are the following nondimensional groups,

$$\Lambda=\frac{T_i}{T_f}\;, \quad \Gamma=\frac{\rho_c}{\ell}, \quad \Psi=\frac{T_m}{T_f}, \quad \Phi=\frac{d}{U\,T_f}, \tag{17}$$

where, $\Lambda = f(\rho_a,\rho_m,d,\ell,U,T_f)$, is the ratio of the hair inertial to the flow time scale, $\Gamma = f(\rho_a,d,\ell,U,E)$ is the ratio of the hair reference radius of curvature to hair length, $\Psi = f(T_f,E,\gamma)$ is the ratio of the material relaxation to the flow time scale, and $\Phi = f(d,U,T_f)$ is the ratio of the steady flow time scale d/U to the unsteady flow time scale T_f. We also find a secondary dependence on the reference hair Reynolds number

$$\mathrm{Re}_0=\frac{d\,U}{\nu} \tag{18}$$

and Φ through the drag coefficient, since $\mathrm{Re}_\xi = \mathrm{Re}_0\,|u - \Phi r_t|d/\nu$.

We note that Φ is obtained from the transformation of the terms that compare relative motion between the body and the flow ($u_r = u - \Phi\, r_t$ and $a_r = u_t - \Phi\, r_{tt}$, defined in Section 2.3). Interestingly, if $T_f = 1/\omega$, where ω is a characteristic frequency (as with an oscillatory flow), the group Φ becomes the inverse of the Keulegan-Carpenter number (8). Replacing T_f with the steady flow time scale (i.e. if the flow is steady) d/U gives $\Phi = 1$, reducing the parameter dependence by one group.

With prior knowledge of the hair structure flow environment (that is, specifying U, T_f, ρ_a and ν), the hair aspect ratio, and the hair density, we determine the parameters $(\Lambda, \Phi, R, \mathrm{Re}_0)$. Following the small displacement assumption ($r < 0.1\,\ell$), $\rho_c >> \ell$ so that in general $\Gamma >> 1$. This leaves the magnitude of Ψ undetermined, which is the only group dependent on the material damping parameter, γ. Indeed, the material selected to fabricate the artificial hair structure (e.g. carbon, polymers or metals) leads to a range of γ. Thus, the value of Ψ may vary several orders of magnitude depending on the material selection. We will investigate this dependence in Section 4.2.

3. Details of Simulation

3.1. Finite Element Solution of the Fluid Model

Solutions to the flow problem (1) were approximated using the characteristic Galerkin finite element method (Zienkiewicz et al., 2005) with the software package FreeFEM++ (Hecht et al., 2008). We set the cylinder diameter, $D =$ 0.10 m and the maximum inlet velocity, $U_{in} = 0.0794$ m/s so that $\mathrm{Re}_{cyl} = 500$. The inlet acceleration parameter was $\lambda = 15$. We discretized in space with the Taylor-Hood pair and integrated with a constant time step of 10^{-5} s over the time interval $0 \leq tU_{in}/D \leq 3.97$ with a first order backward-step method. We will further denote the nondimensional fluid time, tU_{in}/D, as t^*. The domain was meshed with an unstructured triangulation and refined at the cylinder wall

to help resolve the flow velocity near the hair. The final grid was composed of 30532 elements in the pressure grid, and 59943 elements in the velocity grid.

3.2. Finite Element Solution of the Hair Model

We consider hair-like structures with a 100:1 aspect ratio ($\ell = 1e-3$ m, $d = 1e-5$ m) so that hair length is $1/100th$ the half cylinder diameter, D. Hair density and elastic modulus were selected as $\rho_m = 10^3$ kg/m^3 and $E = 10^7$ Pa, based on the value of polymers Gere (2001). With the flow properties above (Section 3.1), this leads to $\Lambda = 0.415$, $\Gamma = 1.34 \times 10^2$, $\Phi = 1.89 \times 10^{-3}$ and $\mathrm{Re}_0 = 5.00 \times 10^{-2}$. We explore the effect of Ψ (the ratio of the hair material relaxation to characteristic flow time scale for $\Psi \sim 10^{-3}$ to 10^3) on the time accurate reception of near surface flow velocity via hair tip deflection and resultant moment.

To simulate the motion of each hair, we multiplied the nondimensional hair model (15) by a test function $\phi(\xi)$ and integrated by parts twice to look for solutions $r(t,\xi) \in L^2(0,T;V)$ such that

$$\left[\frac{2}{R}\Lambda^2 + \frac{\pi}{2}\Phi C_m\right](r_{tt}\,,\,\phi) + \frac{\Gamma}{R}(r_{t\xi\xi} + \Psi\, r_{\xi\xi}\,,\,\phi_{\xi\xi}) - (g(t,\xi,r_t,u,u_t)\,,\,\phi) = 0, \quad \forall \phi \in V, \tag{19}$$

where $V = \{\phi \in H^2(0,L)\,|\,\phi(0),\, \phi_\xi(0) = 0\}$, and $(f,g) = \int_0^L f(x)\,g(x)\,dx$ denotes the standard L^2 inner product. In the finite element discretization of (19), we looked for approximate solutions $r^h \in V^h$ such that

$$\left[\frac{2}{R}\Lambda^2 + \frac{\pi}{2}\Phi C_m\right]\left(r^h_{tt}\,,\,\phi^h\right) + \frac{\Gamma}{R}\left(r^h_{t\xi\xi} + \Psi\, r^h_{\xi\xi}\,,\,\phi^h_{\xi\xi}\right) - \left(g(t,\xi,r^h_t,u,u_t)\,,\,\phi^h\right) = 0, \quad \forall \phi \in V, \tag{20}$$

where $V^h \subset V$ is a finite dimensional space spanned by cubic B-splines $\{\phi(\xi)\}_{i=1}^N$ on a grid defined over $(0,1)$ and

$$r(t,\xi) \approx r^h(t,\xi) = \sum_{i=1}^{N} R_i(t)\phi_i(\xi).$$

Substituting r^h into the finite element form (20) gives the second-order system of nonlinear ordinary differential equations

$$M\,R_{tt} + A\,R_t + C\,R = F(t, R_t, u, u_t) \tag{21}$$

to be solved for $R = [R_1(t) \ldots R_N(t)]$.

The finite element discretization (21) was integrated in time with a constant step backward differentiation formula (BDF), where the order of integration ($2nd$ to $4th$ order) was selected on the basis of numerical stability. At each time step, a modified Newton iteration with relative and absolute tolerances set to 10^{-10} was applied to solve the fully discretized system. Time step sizes of $\Delta t \sim 1 \times 10^{-3}$ and a mesh of 64 nodes were found to provide numerical convergence.

4. Results and Discussion

4.1. Simulation of the Impulsively Started Flow Over the Half Cylinder

Figure 8 contains two velocity magnitude snapshots that illustrate the unsteady separation at $t^* = 0.51$ and $t^* = 2.01$, respectively. In Figure 8 (*Top*), the point of zero wall shear stress is in upstream transit and a region of clockwise recirculation is confined near the cylinder surface. In Figure 8 (*Bottom*) the location of the point of zero wall shear stress has come to equilibrium at 75° while the recirculation has grown to a size on the order of the cylinder.

Upstream of the large clockwise recirculation (Figure 8 (*Bottom*)) between 33° and 74°, we observe a pair of weak counter rotating vortices, illustrated in Figure 9. The onset of the counter rotating pair appears near $t^* = 1.0$ and is unsteady in the separated flow throughout the remainder of the simulation ($1.0 \leq t^* \leq 3.97$) . Although, not present in the classical impulsively started cylinder analysis (see Schlichting Schlichting and Gersten (2000)), evidence of this phenomena has been reported in previous finite element solutions of the half cylinder Gresho and Sani (1998) and is possibly an outcome of the artificial boundary conditions. Whether the counter rotating pair is an artifact of the

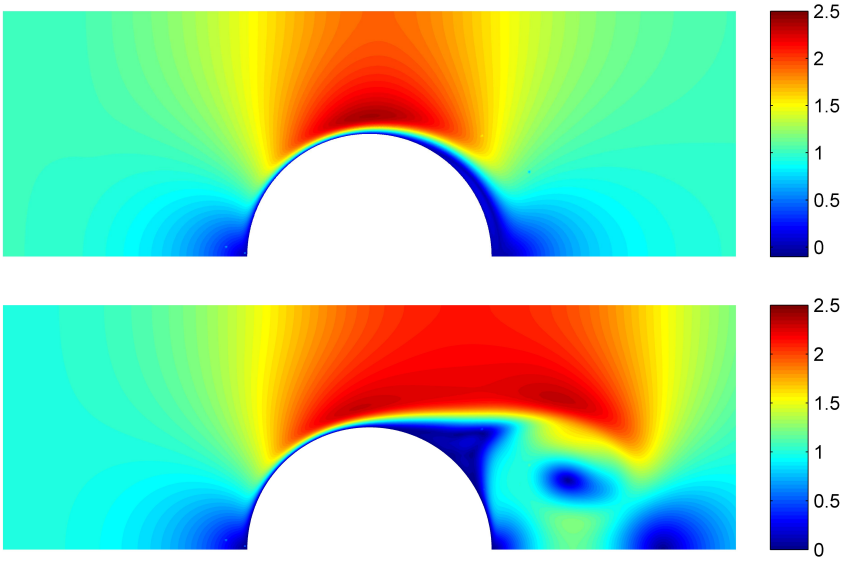

Figure 8: (**Top**) Velocity magnitude, $|\mathbf{u}|/U_{in}$, snapshot at $t^* = 0.51$ with a thin region of clockwise recirculating flow on right-hand (downstream) side of cylinder (**Bottom**) Velocity magnitude snapshot at $t^* = 2.01$ with clockwise recirculation grown to the order of cylinder size

artificial domain (Figure 4) or an actual physical phenomena, for the purpose of this study we find the counter rotating pair as an interesting flow phenomena to investigate from the response of an array of hair-like structures.

By visualizing the near-surface flow velocity and wall shear stress, we obtain a representation of the above described flow phenomena (Figures 10 and 11). Figure 10 is a plot of the nondimensional flow velocity at $0.01\,D$ above and tangent to the half cylinder surface. In polar coordinates, Figure 10 is a plot of the tangential velocity, $u_\phi = u_\phi(t, r, \phi)$, where $r = 1.01\,D$ is the radial coordinate and $\phi = 1, 2, \ldots, 179°$ for $0 \leq t^* \leq 3.97$ taking the half-cylinder vertex as the origin. A similar visualization is obtained from the wall shear stress (Figure 11), which was approximated with a first order finite difference at each $\phi = 1, 2, \ldots, 179°$, equivalent to scaling the near surface velocity $u_\phi(t, r, \phi)$ at $r = 1.002D$ by $\mu/\Delta\xi$, where $\Delta\xi = 0.002\,D$ and μ is the molecular viscosity.

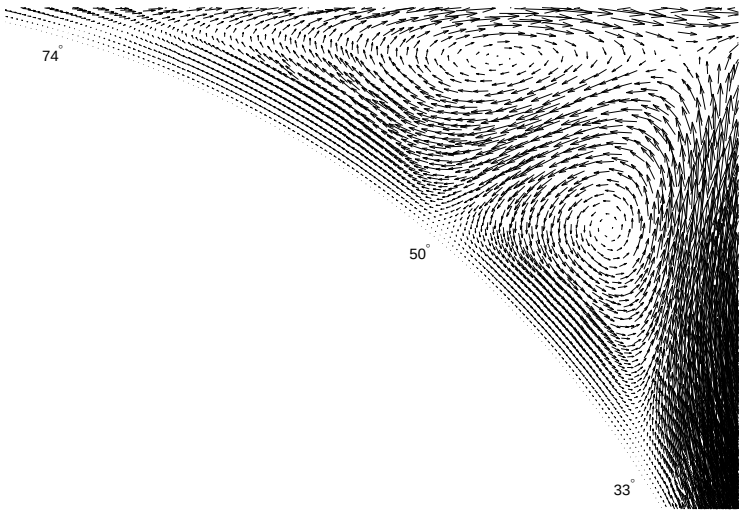

Figure 9: Velocity vector plot showing counter rotating swirl pattern at $t^* = 1.50$ between 33° and 74°

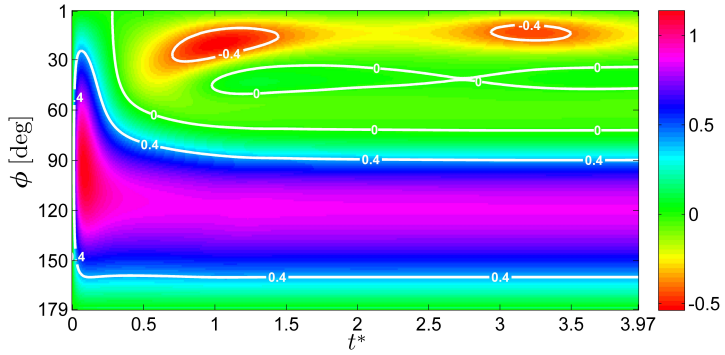

Figure 10: Dimensionless flow velocity (colorbar) tangent to half cylinder surface at a distance $1/100th$ the half cylinder diameter plotted in degree increments for $\phi = 1°$ to 179° for $0 \leq t^* \leq 3.97$

Over the distance $1.0\,D \leq r \leq 1.002\,D$, the velocity profile is roughly linear. At distances further away from the cylinder wall, the linear form of the velocity profile is lost, decreasing the degree of similarity between the images of flow

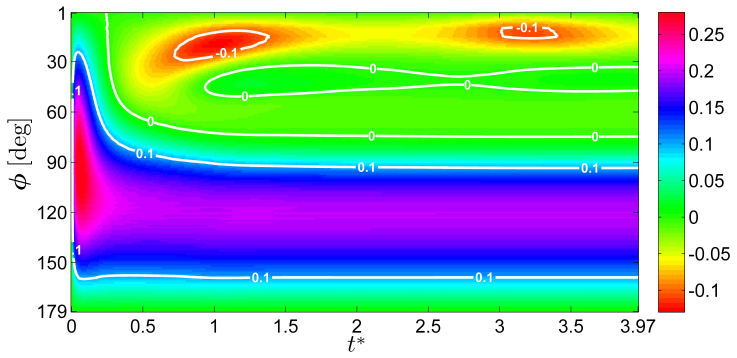

Figure 11: Dimensionless wall shear stress (colorbar) on the half cylinder plotted in degree increments $\phi = 1^\circ$ to 179° for $0 \leq t^* \leq 3.97$

velocity and wall shear stress. Thus, only for sufficiently short hairs will the images of the incident flow velocity and wall shear stress be similar.

For reference, iso-contours interpolated from the data in Figures 10 and 11 are superimposed. From the above *flow footprints*, we may infer the space and time location of the phenomena associated with the unsteady separation. For $t^* < 0.27$, we observe the initially attached boundary layer flow, with maximum tangential velocity near $\phi = 90^\circ$. At $t^* = 1.0$ and $\phi = 1^\circ$ a zero valued contour originates and sharply move upstream, coming to equilibrium at approximately $\phi = 75^\circ$ (Figures 10 and 11). In Figure 10, the zero contour indicates the approximate location of an interface between forward and reversed flow. Here, only the radial flow velocity may have nonzero value. In Figure 11, the interpolated zero-valued contour is the approximate location of the point of zero wall shear stress.

Downstream of the zero contours, the flow is separated with the negative tangential velocity and wall shear values indicating reversed flow. Within the separated flow, a positive valued region is observed beginning at $t^* = 1$ then growing and contracting between 30° and 60°. This region is the footprint of the weak clockwise rotating swirl shown in Figure 9. Thus, at any instant in the separated flow, the location of each vortex is indicated by the space between the zero-valued contours. Upstream of 75°, the forward laminar attached boundary

layer flow develops and is shown coming to equilibrium.

4.2. Analysis of an Individual Hair Structure

We begin by describing the dynamic response of hair 15 (placed at 15° on the half-cylinder, Figure 3). Recall that Ψ is the ratio of the material relaxation time scale γ/E to the unsteady flow time scale $T_f = 1/\lambda$ and is determined independently of the other nondimensional groups (17) by the material damping parameter, γ. We first simulate the motion of hair 15 for $\gamma = 10^3$ ($\Psi = 1.5 \times 10^{-3}$). The remaining dimensionless groups are as previously computed, $\Lambda = 0.415$, $\Gamma = 1.34 \times 10^2$, $\Phi = 1.89 \times 10^{-3}$ and $\mathrm{Re}_0 = 5.00 \times 10^{-2}$.

Figure 12 contains plots of the flow velocity at 15° on the half cylinder and normally incident on hair 15, along with the resulting hair displacement and velocity. We note that throughout this section, the variables displayed

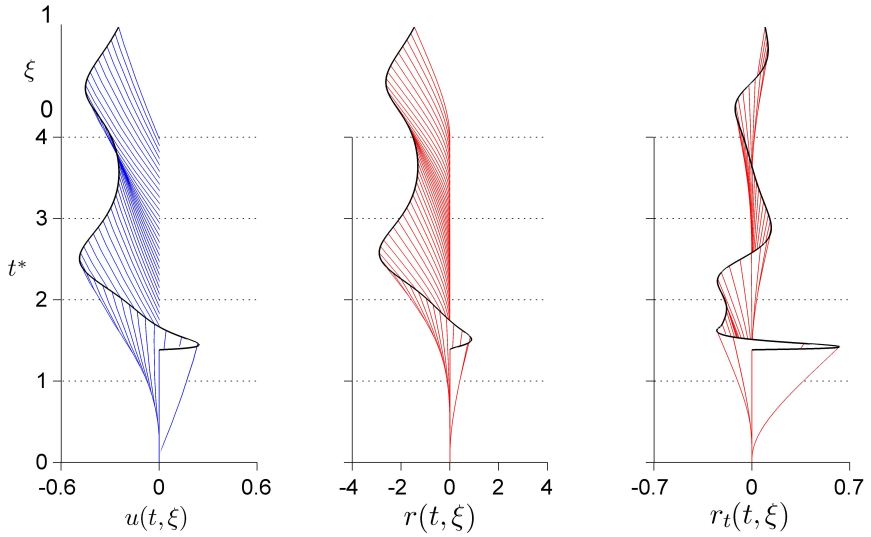

Figure 12: Dimensionless flow velocity (*left*) incident on hair 15, resulting hair dimensionless deflection (*middle*) and dimensionless hair velocity (*right*) for $\Psi = 1.5 \times 10^{-3}$ where $\Lambda = 0.415$, $\Gamma = 1.34 \times 10^2$, $\Phi = 1.89 \times 10^{-3}$ and $\mathrm{Re}_0 = 5.00 \times 10^{-2}$

in all plots are nondimensional as defined in Section 2.3. For convenience in comparing the results of this section to the flow data in Section 4.1, we plot

all nondimensional quantities here against the nondimensional flow time, $t^* = tU_{in}/D$, where t is the dimensional time. From Figure 12, we find that hair displacement is in phase and proportional to the flow velocity. To understand this result we consider an order of magnitude analysis of the nondimensional hair model (15).

Following the choice of scales, for case considered in Figure (12), the quantities that multiply the nondimensional coefficients are on the order of one (we note that strictly speaking $u \sim .1$ for hair 15 since $u(t,\xi) \leq 0.5$). It follows that for $\Phi \sim 10^{-3}$, the effect of relative hair motion is negligible ($u - \Phi\, r_t \approx u$ and $u_t - \Phi\, r_{tt} \approx u_t$). Furthermore, the coefficient of the hydrodynamic mass term, $\pi\Phi(1 + C_m)/2 \sim 10^{-3}$ while $C_D(\mathrm{Re}_0) \sim 10^2$ so that drag dominates the hydrodynamic mass force. Thus, the load intensity on the hair structure is effectively, $g(t,\xi) = C_D\, u\, |u|$.

On the left hand side of the nondimensional beam equation (15), within the inertial coefficient we find that hair inertia and added mass forces are on the same order of magnitude ($2\Lambda^2/R \sim \pi\, \Phi\, C_m/2 \sim 10^{-3}$) while the viscoelastic coefficient, $\Gamma/R \sim 1$, so that the remaining forces which determine the response of hair 15 (Figure 12) are the viscoelastic and drag forces,

$$\frac{\Gamma}{R}\,(r_{\xi\xi\xi\xi} + \Psi\, r_{t\xi\xi\xi\xi}) = C_D(u)\, u\, |u|. \tag{22}$$

Finally, since $\Psi \sim 10^{-3} << 1$ the viscous term $\Psi\, r_{t\xi\xi\xi\xi}$ may be dropped leaving,

$$\frac{\Gamma}{R}\, r_{\xi\xi\xi\xi} = C_D(u)\, u\, |u|.$$

Here, the relaxation time $T_m = \gamma/E$ is assumed negligible compared to the flow time scale $T_f = 1/\Lambda$ so that the displacement due to drag is effectively instantaneous. Since drag is a direct function of incident flow velocity, displacement (Figure 12 *middle*) is in-phase with the incident flow (Figure 12 *left*). Furthermore, the reference hair Reynolds number regime ($\mathrm{Re}_0 = 0.05 << 1$) indicates that the drag force has an effectively linear dependence on velocity leading to a displacement proportional to u.

If the relaxation time is sufficiently large, the in-phase response of the hair structure is lost (Figure 13). This is due to a lag in material relaxation as the flow

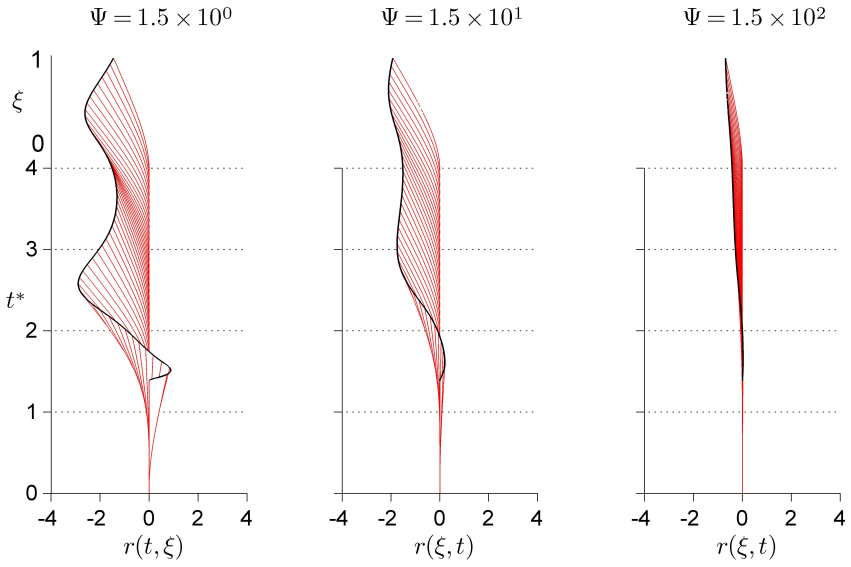

Figure 13: Hair 15 displacement for increasing Ψ where $\Lambda = 0.415$, $\Gamma = 1.34 \times 10^2$, $\Phi = 1.89 \times 10^{-3}$ and $\mathrm{Re}_0 = 5.00 \times 10^{-2}$

velocity changes on the time scale of T_f. Another outcome of an increasing Ψ is a progressively decreasing displacement over any given time period of observation, such as the flow simulation time, $0 \leq t^* \leq 3.97$. This is due to the increasing period of time necessary for the hair structure come to an equilibrium condition (that is, the rate of relaxation $1/T_m$ is small). Clearly, from equation (22) as $\Psi \to \infty$, $r \to 0$ so that the hair becomes static for any finite time scale of observation.

The group Ψ, defined here as the ratio of the time scale of material relaxation to the unsteady flow time scale, T_m/T_f, is effectively the Deborah number (Reiner, 1964) defined as,

$$\frac{\text{Time Scale of Relaxation}}{\text{Time Scale of Observation}}, \tag{23}$$

where the time scale of relaxation refers to a continuous media. The Deborah number is very large in The Pitch Drop Experiment (Edgeworth et al., 1984),

where highly viscous pitch ($\sim 10^{11}$ times that of water) appears frozen to the observer but actually is in the process of dripping through a funnel at the rate of roughly one drop every 10 years. A similar situation is approached as Ψ increases, where from the perspective of the flow the hair appears frozen but is actually dynamic over a relatively much larger time scale. Figure 4.2 summarizes the effect of Ψ on hair displacement. On the basis of the above analysis

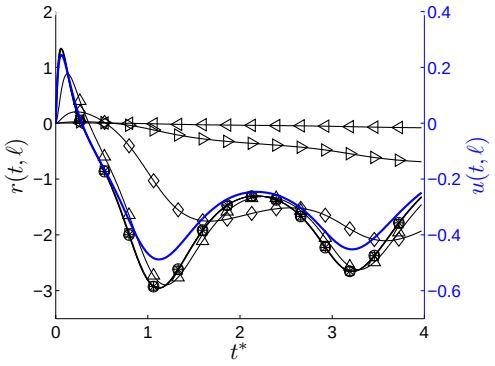

Figure 14: Hair 15 dimensionless tip displacement with incident tip flow velocity where $(-\circ-)$ $\Psi = 1.5\times10^{-3}$, $(-*-)$ $\Psi = 1.5\times10^{-2}$, $(-\square-)$ $\Psi = 1.5\times10^{-1}$, $(-\Delta-)$ $\Psi = 1.5\times10^{0}$, $(-\Diamond-)$ $\Psi = 1.5\times10^{1}$, $(-\circ-)$ $\triangleright = 1.5\times10^{2}$, $(-\triangleleft-)$ $\Psi = 1.5\times10^{3}d$, for $\Lambda = 0.415$, $\Gamma = 1.34\times10^{2}$, $\Phi = 1.89\times10^{-3}$ and $\mathrm{Re}_0 = 5.00\times10^{-2}$

and results, we submit the following principle for hair structures governed by equation (22): *Changes in flow velocity (acceleration) may be observed from hair displacement (velocity) if* $\Psi << 1$.

In addition to displacement, an incident flow along the length of a hair will induce a resultant moment. Figure 4.2 is a plot of M (16) vs t^* for $\Psi = 1.5\times10^{-3}$ to 1.5×10^{3}. Despite the wide range of hair displacements shown above, the resultant moment at the base of the hair appears insensitive to Ψ, and in-phase and roughly proportional to the tip flow velocity.

Recall that the dimensionless moment data in Figure (4.2) was determined from,

$$M = r_{t\xi\xi}(t,0) + \Psi\, r_{\xi\xi}(t,0) \tag{24}$$

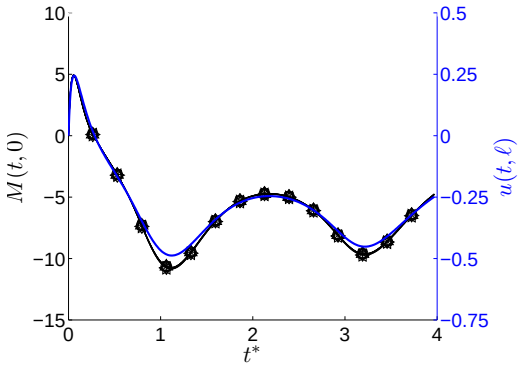

Figure 15: Hair 15 dimensionless resultant moment (*Right*) with incident tip flow velocity where $(-\circ-)$ $\Psi = 1.5 \times 10^{-3}$, $(-*-)$ $\Psi = 1.5 \times 10^{-2}$, $(-\square-)$ $\Psi = 1.5 \times 10^{-1}$, $(-\Delta-)$ $\Psi = 1.5 \times 10^{0}$, $(-\Diamond-)$ $\Psi = 1.5 \times 10^{1}$, $(-\circ-)$ $\triangleright = 1.5 \times 10^{2}$, $(-\triangleleft-)$ $\Psi = 1.5 \times 10^{3} d$, for $\Lambda = 0.415$, $\Gamma = 1.34 \times 10^{2}$, $\Phi = 1.89 \times 10^{-3}$ and $\mathrm{Re}_0 = 5.00 \times 10^{-2}$

by solving the hair PDE (15). Comparing equation (16) to (22), we find that under the assumptions of the simplified hair equation (22) (negligible hair inertia, added mass force, hydrodynamic mass force, and relative hair motion) moment is directly and solely a function of drag. Thus, we may directly compute resultant moment from flow velocity without solving (15) as follows. Let F_D be the total drag on the hair structure which may be determined as,

$$F_D = \int_0^\ell g(t,\xi)\, d\xi$$

where $g = C_D\, u\, |u|$. Then, the resultant moment may alternatively be computed as

$$M(t) = F_D\, \bar{\xi}$$

where

$$\bar{\xi} = \frac{\int_0^\ell g(t,\xi)\, \xi\, d\xi}{\int_0^\ell g(t,\xi)\, d\xi}$$

is the center of mass of g. This leads to the following equation for instantaneous moment,

$$M(t) = \int_0^\ell C_D(u)\, u\, |u|\, \xi\, d\xi. \tag{25}$$

Equation (25) was previously considered by Dickinson (2010) in the sensitivity analysis of the hair sensor in steady boundary layer flows.

4.3. Hair Array Response to the Unsteady Flow Separation

Recall that a main objective of this study was to determine how hair material properties affected the time accurate measurement of near surface flow topology. We now present the complete hair array response to the impulsively started flow over a cylinder simulation (Section 2). As in the prior section, all quantities plotted are dimensionless as previously defined.

Figure 16, contains plots of dimensionless tip deflection, $r(t, \ell)$, against angular location on the cylinder and time t^* for $\Psi << 1$ and $\Psi >> 1$. As expected following the discussion in the previous section, when $\Psi << 1$ the tip deflection of each hair is approximately proportional to and in-phase with the evolution of the near surface flow velocity. As a result, comparison of Figure 16 (*Top*) with Figure 10 confirms a time accurate representation of the flow topology. Furthermore, Figure 16 (*Top*) is also similar to the wall shear image (Figure 11) due to the similarity with the surface velocity (Figure 10). As discussed in Section 4.1, this follows from the short length of the hair structure.

Conversely, a distorted image is returned from the hair array possessing a larger time scale of relaxation relative to the time scale of the flow ($\Psi >> 1$).

The array moment response also provides a similar visualization of the near surface flow velocity and wall shear stress (Figure 17).

It is important to note that the values Λ, Γ, Φ and Re_0 dictated by other flow scenarios may not lead to the same set of moment and displacement behaviors that are reported in this section. This is especially true when material damping is small, as hair velocity and acceleration may lead to significant hair inertia, added mass forces, hydrodynamic mass forces, or forces due to relative hair motion. Thus, at present the above results should be considered valid only for hair structures governed by equation (22) where internal viscoelastic forces are balanced by drag. Still, it may be possible to enforce the validity of (22) by choosing a material with sufficiently large Ψ so that $r, r_t, r_{tt} \to 0$. Then, the

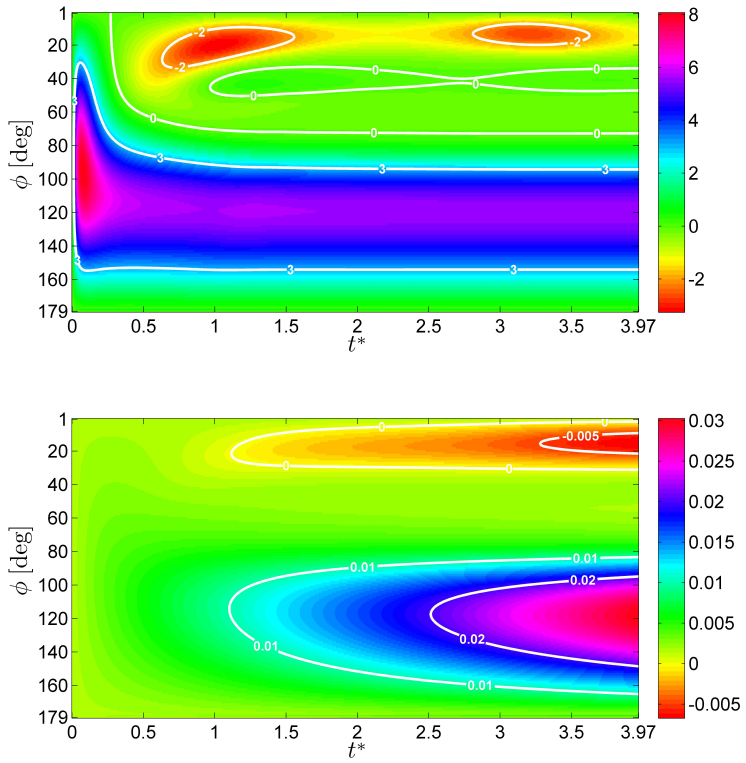

Figure 16: Array dimensionless tip displacement (colorbar) in the unsteady separation over the half-cylinder for $\Psi \sim 1.5 \times 10^{-3}$ (*Top*) and $\Psi \sim 1.5 \times 10^{3}$ for each hair at $\phi = 1^\circ$ to 179° for $0 \leq t^* \leq 3.97$

nondimensional hair model (15) reduces to (22) with hydrodynamic mass term $\pi\Phi(1 + C_m)/2\, u_t$ on the right hand side. If u_t is out of phase with u, as with an oscillatory flow, the forcing is potentially no longer in phase with u so that the results established here do not apply. Thus, to ensure the simplified hair models (22) and (25) are valid, Ψ must be sufficiently large and $\pi\Phi(1 + C_m)/2$ must be much less than C_D.

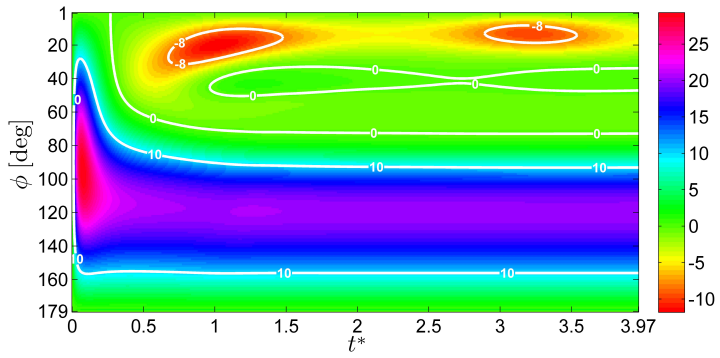

Figure 17: Array dimensionless hair moment (colorbar) response in the unsteady flow separation over the half-cylinder for hairs at $\phi = 1°$ to $179°$ for $0 \leq t^* \leq 3.97$

5. Summary

We investigated the effect of material properties on the visualization of near surface flow velocity patterns with an array of flexible hair-like structures. For this, we proposed a fluid-structure reaction model of the individual hair structure and simulated a hair array response in a laminar unsteady flow separation.

Through a nondimensional analysis of the hair model, we identified and discussed five nondimensional groups that directly determined the hair response. Within the regime of the unsteady separation (Re_{cyl}=500), we found that internal viscoelastic forces and drag forces dominated hair inertia, added mass, and hydrodynamic mass forces. In this situation, we predict:

1. Hair tip displacement will be in-phase and roughly proportional to a measure of the incident flow velocity when the time scale of hair material relaxation is small compared to the incident flow time scale ($\Psi << 1$).
2. Hair resultant moment will be in-phase and roughly proportional to a measure of the incident flow velocity regardless of the value of Ψ.

Here, the flow velocity measure considered was incident velocity at the hair tip.

With the above predictions, we demonstrated a time and space accurate representation of the surface flow topology associated with an unsteady separation

though the tip deflection and moment response of a hair array. The hair array was shown to provide accurate visualizations of all aspects of the unsteady flow separation including regions of reverse flow, the location of the point of zero wall shear stress, the space and time development of attached boundary layer flows, and movement and position of near wall vortices. For the length of hairs considered here ($1/100th$ the cylinder diameter), we also found that the visualization of the near surface flow topology was strikingly similar to the image of wall shear stress.

Future work will focus on the forces present and resulting hair behavior in purely oscillatory flow conditions. Additionally, we will numerically investigate hair sensors in guidance, navigation, and control applications on small scale air vehicles.

Acknowledgments

We would like to thank Susanne Sterbing-D'Angelo for editing comments and information on bat hair receptors. We also would like to thank Sharon Swartz for many interesting conversations regarding bat hair receptors. Finally we would like to thank Cody Ray, Ehsan Shams, Dave Willis and Arun Wikiramasuriya for their editing comments. This research is supported in part by the Air Force Office of Scientific Research through grants FA9550-05-1-0041 and FA9550-07-1-0540.

References

Bathellier, B., Barth, F., Albert, J., Humphrey, J., 2005. Viscosity-mediated motion coupling between pairs of trichobothria on the leg of the spider *Cupiennius salei*. J Comp Physiol A 191, 733–746.

Billone, M., Raynor, S., 1973. Transmission of radial shear forces to cochlear hair cells. J Acoust Soc Am 54, 1143–1156.

Brücker, C., Bauer, D., Chaves, H., 2007. Dynamic response of micro-pillar sensors measuring fluctuating wall-shear-stress. Exp. Fluids 42, 737–749.

Brüker, C., Spatz, J., Schróder, W., 2005. Wall shear stress imaging using micro-structured surfaces with flexible micro-pillars. Exp. Fluids 39, 464–474.

Cebeci, T., 1979. The laminar boundary layer on a circular cylinder stated impulsively from rest. J Comput Phys 31, 153–172.

Crowley, G., Hall, L., 1994. Histological observations on the wing of the grey-headed flying-fox (Pteropus-Poliocephalus) (Chiroptera, Pteropodidae). Aust J Zool 42, 215–231.

Davis, J., 1987. Dynamics of Continuous Media. Macmillan.

Dickinson, B., 2010. Hair receptor sensitivity to changes in laminar boundary layer shape. Bioinspr Biomim 5, 1–11.

Dijkstra, M., van Baar, J., Wiegerink, R., Lammerink, T., de Boer, J., Krijnen, G., 2005. Artificial sensory hairs based on the flow sensisitve receptor hairs of crickets. J Micromechs Mircoeng 15, S132–S138.

Edgeworth, B., Dalton, B., Parnell, T., 1984. The pitch drop experiment. Eur J Phys 5, 198–200.

Engel, J., Chen, J., Bullen, D., Liu, C., 2005. Polyurethane rubber as MEMS material: characterization and demonstration of an all polymer two-axis artificial haircell flow sensor. In: 18th IEEE International Conference on Micro Electro Mechanical Systems.

Engel, J., Chen, J., Liu, C., Bullen, D., 2006. Polyurethane rubber all-polymer artificial hair cell sensor. J Microelectromech Sys 15, 729–736.

Fletcher, N., 1978. Acoustical response of hair receptors in insects. J. Comp. Physiol. 127, 185–189.

Gere, J., 2001. Mechanics of Materials. Brooks/Cole.

Gnanimanickam, E., Sullivan, J., 2008. Image based sensor for distributed wall shear stress measurement. In: 46th AIAA Aerospace Sciences Meeting and Exhibit.

Gresho, P., Sani, R., 1998. Incompressible flow and the finite element method - advection-diffusion and isothermal laminar flow. John Wiley and Sons.

Hagedoorn, B., 2008. Viscous coupling between bio-inspired hair-sensors. Master's thesis, University of Twente.

Hecht, F., Pironneau, O., Le Hyaric, A., Ohtsuka, K., 2008. Freefem++ Version 2.23-2. Http://www.freefem.org/ff++.

Heywood, J., Rannacher, R., Turek, S., 1996. Artificial boundaries and flux and pressure conditions for the incompressible Navier-Stokes equations. Int J Numer Meth Fl 22, 325–352.

Honji, H., 1981. Streaked flow around an oscillating circular cylinder. J Fluid Mech 107, 509–520.

Hubel, T., Riskin, D., Swartz, S., Breuer, K., 2010. Wake structure and wing kinematics" the flight of the lesser dog-faced fruit bat, *Cynopterus brachyotis*. J Exp Biol 213, 3427–3440.

Humphrey, J., Devarakonda, R., Iglesias, R., Barth, F., 1993. Dynamics of arthropod filiform hairs. I. Mathematical hair modeling of the hair and air motions). Phil. Trans. R. Soc. Lond. B 340 (1294), 423–444.

Inman, D., 2008. Engineering Vibration. Pearson Prentice Hall.

Jana, A., Raman, A., Dhayal, B., Tripp, S., Reifenberger, R., 2007. Microcantilever mechanics in flowing viscous fluids. Appl Phys Lett 90.

Keulegan, G., Carpenter, L., 1958. Forces on cylinders and plates in an oscillating fluid. J Res Nat Bureau of Standards 60, 423–440.

Lamb, H., 1911. On the uniform motion of a sphere through a viscous fluid. Phil Mag 21, 112–121.

Lissaman, P., 1983. Low-reynolds-number airfoils. Ann Rev Fluid Mech 15, 223–239.

Mangalam, A., Mangalam, S., Flick, P., 2008. Unsteady aerodynamic observable for gust alleviation and flutter suppression. In: 26th AIAA Applied Aerodynamics Conference.

Mangalam, A., Moes, T., 2004. Real-time unsteady loads measurements using hot-film sensors. In: 22nd Applied Aerodynamic Conference and Exhibit.

Mangalam, A., Moore, G., Berg, D., Blaylock, M., Rumsey, M., 2010. Real-time aerodynamic observable for wind turbine applications. In: 51st AIAA/ASME/ASCE/AHS/ASC Structures, Structural Dynamics, and Materials Conference.

Morison, J., O'Brien, M., Johnson, J., Schaaf, S., 1950. The force exerted by surface waves on piles. Petroleum Transactions, AIME 189, 149–154.

Mueller, T., DeLaurier, J., 2005. Aerodynamics of small vehicles. Ann Rev Fluid Mech 35, 89–111.

Ozaki, Y., Yasuda, T. O. T., Shimoyama, I., 2000. An airflow sensor modeled on wind receptor hairs of insects. In: The 13th International Conference on Micro-Electro-Mechanical Systems.

Prandtl, L., 1952. Essentials of fluid dynamics. Halfner Publishing Company, New York.

Reiner, M., 1964. The deborah number. Physics Today 17, 62.

Sarpkaya, T., 1986. Force on a circular cylinder in viscous oscillatory flow at low Keulegan-Carpenter numbers. J Fluid Mech 165, 61–71.

Sarpkaya, T., Issacson, M., 1981. Mechanics of wave forces on offshore structures. Van Nostrand Reinhold Company Inc.

Schlichting, H., Gersten, K., 2000. Boundary Layer Theory. Springer.

Schmitz, G., Brüker, C., Jacobs, P., 2005. Manufacture of high-aspect-ratio micro-hair sensor arrays. J Micromech Microeng 15, 1904–1910.

Sears, W., Telionis, D., 1975. Boundary-layer separation in unsteady flow. SIAM J Appl Math 28, 215–235.

Shimozawa, T., Kanou, M., 1984. Varieties of filiform hairs: range fractionation by sensory afferents and cercal interneurons of a cricket. J Comp Physiol A 155, 485–493.

Shyy, W., Berg, M., Ljungqvist, D., 1999. Flapping and flexible wings for biological and micro vehicles. Prog Aerosp Sci 35, 455–506.

Sterbing-D'Angelo, S., Chadha, M., Moss, C., 2008. Representation of the wing membrane in somatosensory cortex of the bat, *Eptesicus fuscus*. In: Neurosci. Abstr. 370.4.

Sumer, B., Fredsøe, J., 2006. Hydrodynamics Around Cylindrical Structures. World Scientific.

Tautz, J., 1977. Reception of medium vibration by thoracal hairs of caterpillars of *Barathra brassicae* l. (lepidoptera, noctuidae). J. Comp. Physiol. 118, 13–31.

Yang, Y., Chen, N., Tucker, C., Engel, J., Pandya, S., Liu, C., 2007. From artificial hair cell sensor to artificial lateral line system: development and application. In: 20th IEEE International Conference on Micro Electro Mechanical Systems.

Zienkiewicz, O., Taylor, R., Nithiarasu, P., 2005. The finite element method for fluid dynamics. Elsevier Butterworth-Heinemann.

Zook, J., 2005. The neuroethology of touch in bats: cutaneous receptors of the wing. In: Neurosci Abstr 78.21.